View metadata, citation and similar papers at core.ac.uk

brought to you by CORE

provided by HAL-INSU

WAVANGLET: an efficient supervised classifier for hyperspectral images

Frédéric Schmidt, Sylvain Douté, Bernard Schmitt

To cite this version:

Frédéric Schmidt, Sylvain Douté, Bernard Schmitt. WAVANGLET: an efficient supervised classifier for hyperspectral images. IEEE Transactions on Geoscience and Remote Sensing, Institute of Electrical and Electronics Engineers, 2007, 45 (5), pp.1374–1385. <10.1109/TGRS.2006.890577>. <hal-00325458>

HAL Id: hal-00325458

https://hal.archives-ouvertes.fr/hal-00325458

Submitted on 29 Sep 2008

HAL is a multi-disciplinary open access archive for the deposit and dissemination of scientific research documents, whether they are published or not. The documents may come from teaching and research institutions in France or abroad, or from public or private research centers.

L'archive ouverte pluridisciplinaire **HAL**, est destinée au dépôt et à la diffusion de documents scientifiques de niveau recherche, publiés ou non, émanant des établissements d'enseignement et de recherche français ou étrangers, des laboratoires publics ou privés.

WAVANGLET: an efficient supervised classifier for hyperspectral images

Schmidt Frédéric, Douté Sylvain and Schmitt Bernard

Laboratoire de Planétologie de Grenoble - CNRS/UJF,
Bâtiment D de Physique, B.P.53 38041 Grenoble Cedex 09,
FRANCE

Keywords : pattern recognition, hyperspectral images, remote sensing, mass treatment, automatic detection, spectral feature recognition and extraction, automatic supervised classification, wavelet filtering.

Abstract*—The new generation of imaging spectrometers on board planetary missions usually produce hundreds to thousands of images a year, each made up of a thousand to a million spectra with typically several hundred wavelengths. Such huge datasets must be analyzed by efficient yet accurate algorithms. A supervised automatic classification method (hereafter called "*wavanglet*") is proposed to identify spectral features and classify images in spectrally homogeneous units.** ***It uses four steps: A. Selection of a library composed of reference spectra; B. Application of a Daubechies wavelet transform to referenced spectra and determination of the wavelet subspace that best separates all referenced spectra; C. In this selected subspace, determination of the best threshold on the spectral angle to produce detection masks. **This application is focused on the martian polar regions that present three main types of terrains: H_2O ice, CO_2 ice and dust. The "*wavanglet*" method is implemented to detect these major compounds on near-infrared hyperspectral images acquired by the OMEGA instrument on board the Mars Express spacecraft. With an overall accuracy of 89%, "*wavanglet*" outperforms two generic methods: Band Ratio (57% accuracy) and Spectral Feature Fitting^{TM} (83% accuracy). The quantitative detection limits of "*wavanglet*" are also evaluated in terms of abundance for H_2O and CO_2 ices in order to improve the interpretation of the masks.**

I. Introduction

In order to understand the current climate on Mars it is necessary to detect, characterize and monitor CO_2 and H_2O ices at its surface (permanent and seasonal deposits) and in its atmosphere (vapor, clouds). The series of images acquired above medium latitudes and the poles by the OMEGA [1] imaging spectrometer on board the Mars Express mission (ESA) represents a unique opportunity to achieve these objectives. At present, its contain more than a hundred visible (VIS) and near infrared (NIR) hyperspectral images taken during different seasons above the north and south polar regions with usually $\sim$100,000 spectra for each image.

We aim to :

1) Evaluate the relevance of each image for volatile molecule studies in terms of fractions covered by CO_2 and H_2O ices.
2) Generate CO_2 and H_2O ice distribution maps.
3) Automatically determine the seasonal condensation and defrost lines and their temporal evolution.
4) Define spectrally homogeneous units of terrain as detection masks, each undergoing a specific physical modeling of the spectra in order to evaluate their surface properties.

Because of the huge volume of data, we need an automatic and efficient algorithm to achieve these goals in a reasonably short calculation time. In supervised classification, the usual way to compare each spectr X of a hyperspectral image and a well-known reference spectrum E is to calculate their Spectral Angle (SA) [2] in the n dimensional base (n=the number of channels) which is equivalent to the correlation coefficient. However, this method is not robust enough to classify the polar terrains because of the slightly degraded signal to noise ratio of the spectra mostly acquired at high incidence angles. Furthermore, gaseous CO_2 and H_2O present in the atmosphere add absorption features that sometimes partly overlap their solid counterparts. Finally, variations of the physical properties of the ices (e.g. grain size) and variations of geometrical illumination conditions induce non-linear variations of the absorption band intensity across the studied scene that are impossible to unravel using a linear Spectral Angle method.
Therefore we propose a supervised classification method called *wavanglet*. It defines a more effective way of measuring the spectral angle between the image spectrum X and the reference spectrum E in a wavelet transform domain. The reference is usually an image end-member or a synthetic spectrum that non-ambiguously characterizes the compound to be detected, e.g. CO_2 or H_2O ice owing to their distinctive absorption bands. Similar methods have already been evaluated in remote sensing. The use of wavelets for pattern recognition was already proposed by [3], [4] and their efficiency is better than that provided by other techniques such as Principal Component Analysis and Fourier Transforms [5]. Experimental studies have shown that the performance of wavelets in classification is very good for vegetation detection with AVIRIS (Airborne Visible/Infrared Imaging Spectrometer) data [6] and hyperspectral data collected at ground level [7].
The use of unsupervised classification methods like PCA [8] or hierarchical clustering [9] is limited when processing large datasets because such methods are computer intensive. Furthermore they do not take advantage of the a priori knowledge we may have concerning planetary surfaces and atmospheres. Finally they classify an image according to multiple chemical, physical and structural information that are combined. Thus the classification can be difficult to interpret in terms of chemical composition only, a problem that we do not encounter with *wavanglet*.

This paper is divided into four sections. In the first , we provide background information necessary to introduce the *wavanglet* method and the OMEGA dataset on which we will base our classification experiments. We also describe comparable standard methods that already exist: Band Ratio[10], [11], Spectral Angle Mapper [2], and Spectral

Feature Fitting^{TM}[12]. The second section presents the different steps followed by our method. Next, we will perform a comparative experiment between *wavanglet* and two standard methods based on performance (overall accuracy, separability between classes, multiple end-members and possible overlapping signatures, mass processing feasibility and calculation time). Finally, in the particular case of the OMEGA polar images, we evaluate quantitative detection limits in terms of abundance for H_2O and CO_2 ices. We also determine how these limits vary with the coexistence mode of the ices, their main physical parameters (e.g. granularity) and the incidence angle of the observation. For this, we use synthetic data.

II. Background information

A. OMEGA instrument

The OMEGA instrument [1] is an imaging spectrometer on board the Mars Express mission (MEX - ESA). Its spatial resolution varies from 350 meters up to 4 kilometers depending on the observation altitude. The instrument has three distinct spectral channels designated V, C and L. Table I summarizes the spectral range, number of spectels and spectral resolution for each. Unlike the V channel, the C and L channels are particularly relevant to our studies since they sample numerous absorption bands distinctive of CO_2 and H_2O in their solid state. After calibration, the dimensionless physical unit used to express the spectra is the reflectance: the irradiance leaving each pixel toward the sensor divided by the solar irradiance at the ground. Each pixel is characterized by a spectrum of 256 spectels organized according to increasing wavelength, the corresponding index going from 0 to 255. The name of each observation is coded as ORBXXXX_Y where XXXX is the orbit number and Y the observation number.

B. Wavelet transform (WT)

Our signals are modeled by finite energy functions of the **H** Hilbert space with the usual norm of the $L^2(\mathbb{R})$ Banach space and the usual inner product $\langle\ ;\ \rangle$. As the Fourier transform is a projection on an orthogonal base made of orthogonal sine and cosine functions, the wavelet transform is a projection into a new base made of orthogonal wavelets. Each wavelet is built by scaling and shifting a single "mother" wavelet [13]. Consequently, a wavelet is defined by a mother pattern, a scale "s" and a position "p".

The mother wavelet is:

- a function:
$$\Psi \in L^2(\mathbb{R}) \quad (1)$$
- with a zero average:
$$\int_{-\infty}^{+\infty} \Psi(x)dx = 0 \quad (2)$$
- centered in the neighborhood of $t = 0$
- and normalized such that:
$$\|\Psi\| = 1 \quad (3)$$
- which could be a base of $L^2(\mathbb{R})$
- which could have the orthonormal property: $\forall(s,p,s',p'),\langle\Psi_{s,p};\Psi_{s',p'}\rangle = \delta_{s,s'}.\delta_{p,p'}$

The originality of wavelets compared to the usual sine and cosine functions, is that each base function is localized. A cosine function, instead, is defined by its period and its phase, and is present throughout the entire signal.

The wavelet transform WE(s,p) of the signal-vector E(x) is:

$$WE(s,p) = \langle E, \Psi_{s,p}\rangle = \int_{-\infty}^{+\infty} E(x)\frac{1}{\sqrt{s}}\Psi^*(\frac{x-p}{s})dx \quad (4)$$

This transformation is linear and can be written by the usual convolution product:

$$WE(s,p) = \int_{-\infty}^{+\infty} E(x)\frac{1}{\sqrt{s}}\Psi^*(\frac{x-p}{s})dx = f \star \Psi_s \quad (5)$$

with $\Psi_s = \frac{1}{\sqrt{s}}\Psi^*(\frac{-x}{s})$

In signal processing, several classes of mother wavelets exist, each with different properties (including non-base and non-orthogonality). We build our *wavanglet* method on an orthonormal base made using the Daubechies wavelet family. The corresponding transform algorithm was specially developed for fast numerical calculation [14]. Faster than the usual wavelet transforms [4], this particular wavelet transform is particularly suitable for the detection and classification of spectral features on large datasets.

The morphology of the Daubechies mother wavelet can be tuned by a parameter - with 4, 16 or 20 as possible values - that depends on the regularity of the signal. If the latter is undersampled, the regularity is low and the best suited mother wavelet must be highly irregular and as short as possible (value 4). If sampling is sufficient, the mother wavelet must be smooth and long (value 20). The OMEGA data correspond to the first case. The discrete WT algorithm transforms a 2^k element vector into a vector of the same length. The counterpart of the spectel index in the wavelet domain will be called the wavelet index. The length 2^k of the vector determines the number of scales k, 8 for OMEGA, due to a spectral dimension of 256. The scale s and position p are not explicitly specified in the output vector but can be easily reconstructed. Each wavelet index corresponds to a unique wavelet with scale s and position p. Different representations of the vector can be used in the wavelet space: for instance the primary output vector or a scale/position scheme. We will use a convenient representation with each scale represented by a 2^k element vector resulting from the superposition of gate functions, one for each wavelet, with a width equal to the scale s, a localization equal to position p and a depth equal to the projection coefficient (see figure ***1***).

Wavelet transforms can be used in spectral pattern recognition as proposed several years ago [3], [4]. The idea is that the wavelet localization and scale respectively correspond to the position and width of a particular spectral feature. Furthermore, the projection coefficient is linked to feature depth. In the case of a hyperspectral planetary image, each

Table I
BASIC SPECTRAL CHARACTERISTICS OF THE OMEGA INSTRUMENT ON BOARD MARS EXPRESS

	V channel	C channel	L channel
Spectral Range (μm)	0.38 to 1.05	0.93 to 2.73	2.55 to 5.1
Number of Samples	96 or 144	128	128
Spectral Resolution (μm)	0.007 or 0.0045	0.013	0.020

Table II
WAVELENGTHS USED IN THE BAND RATIO

Spectel index	35	40	60	75
Wavelength (μm)	1.4286	1.5004	1.7860	1.9973

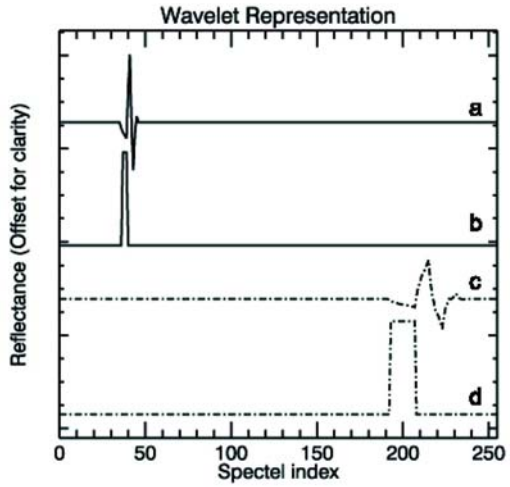

Figure 1. Daubechies wavelet representation. Wavelet No 28 (Scale 5 Position 13) (a) and its representation (b). Wavelet No 73 (Scale 7 Position 10) (c) and its representation (d).

absorption band can be represented by the sum of a limited number of wavelets. In an ideal case, only the projection coefficients for this group of wavelets would differ from zero.

C. Usual classification methods

Many different methods of detection and classification are used in the domain of planetary sciences. We will only summarize three among the most popular.

1) Band Ratio (BR) method: A ratio between two channels of interest can be calculated for all the spectra of an image. For instance, one channel can be chosen in the middle of an absorption band and the other on its far wing (local continuum). In this case, the ratio is straightforwardly linked to the relative band depth. A detection mask can be computed by applying a fixed threshold on the image ratio, above which we consider that the band exists. The threshold can be calibrated by a visual inspection of representative spectra. Sometimes the definition of the band ratio is slightly more refined e.g. the area sustained by the absorption band divided by its continuum. The main advantage of the ratio method is its simplicity. Nevertheless this method is only used for preliminary investigations because of a number of limitations: dependence of hot spectels and sensitivity to non-multiplicative noise, instrumental artifacts and frequent superposition of different absorption bands. This method has already been applied to Mars Express OMEGA data [10], [11].

The band ratio we used for our classification experiments (see section IV-B) is: $\frac{S(40)}{S(35)}(1-\frac{S(75)}{S(60)})$ with the associated wavelengths listed in table II. Spectel index 35 corresponds to a CO_2 solid absorption band and spectel index 40 to a water ice absorption. Spectel index 60 is the continuum and spectel index 75 corresponds to both CO_2 and H_2O absorption bands (see figure 2 for the reference spectra). Terrains with a minimum value of the ratio are composed of dust. CO_2 ice rich terrains are represented by pixels with a high ratio. In between, water ice rich terrains have intermediate values (see figure 4 for the band ratio distribution in one OMEGA observation). An overview of the properties of this method and the results from experiments are reported in table IX.

2) Spectral Angle Mapper$^{\mathrm{TM}}$ (SAM$^{\mathrm{TM}}$): A collection of spectra produced by a given instrument can be represented by a series of vectors each anchored at the origin of an n-dimensional space (n being the number of channels of the instrument). In a usual 3-d Euclidean space, the spectral angle (SA) corresponds to the real angle between the two directions defined by two vectors [2]. In a general n-d space, the SA is a coefficient α between 0 and π radians which determines the proximity of the directions of two vectors E and X.

The spectral angle: $\alpha(E;X) = \arccos\left(\frac{\langle E;X\rangle}{\|E\|.\|X\|}\right) = \arccos\left(cor(E;X)\right)$

The SA is not sensitive to a multiplication factor because it is normalized. This method is often used in remote sensing analysis to compare two spectra (vectors) because the photometric effect is not taken into account. Another way to introduce the SA, is to present it as a correlation coefficient between two random vectors (the spectra) combined with an arc-cosine. As the arc-cosine is a monotonically declining function in the [0, 1] interval, the SA decreases as the normalized correlation

increases. In the extreme case, when the two directions are similar, SA tends to 0 and the normalized correlation tends to 1. When the two vectors are anti-correlated, the correlation coefficient is close to -1 and thus the spectral angle is close to π radians. The intermediary situation is when the angle is $\frac{\pi}{2}$ and the correlation is null.

The value of the SA does not depend on the base used for the vector representation if the new base is orthogonal for the usual scalar product. This means that if the scalar product between two vectors is preserved, the spectral angle is also preserved.

If Φ is a linear operator such as a wavelet transform, e.g. the projection into an orthonormal base of the **H** Hilbert space, we can write:

the Parseval formula:

$$\langle \Phi(E); \Phi(X) \rangle = \langle E; X \rangle \tag{6}$$

and the Plancherel formula:

$$\|\Phi(X)\| = \langle \Phi(X); \Phi(X) \rangle = \langle X; X \rangle = \|X\| \tag{7}$$

thus

$$\alpha \{\Phi(E); \Phi(X)\} = \arccos\left(\frac{\langle \Phi(E); \Phi(X) \rangle}{\|\Phi(E)\| \,.\, \|\Phi(X)\|}\right) \tag{8}$$

$$\alpha \{\Phi(E); \Phi(X)\} = \arccos\left(\frac{\langle E; X \rangle}{\|E\| \,.\, \|X\|}\right) \tag{9}$$

$$\alpha \{\Phi(E); \Phi(X)\} = \alpha(E; X) \tag{10}$$

SAM$^{\mathrm{TM}}$ is an algorithm already implemented in the ENVI® environment [15].

3) Spectral Feature Fitting$^{\mathrm{TM}}$ (SFF$^{\mathrm{TM}}$) *:* Spectral Feature Fitting$^{\mathrm{TM}}$ is a method that compares the spectrum of an image X to a selected reference spectrum E in a least-squares sense [12]. The reference spectrum is scaled to match the image spectrum after continuum removal for both spectra and the root mean square (RMS) error is determined. We choose to express the similarity between X and E by calculating the combined ratio: Scale/RMS. The scale and the RMS are respectively an estimation of the strength of the searched absorption features and of the quality of the fit. A simple threshold can be applied to the ratio to decide if the observed spectrum belongs to the class of the reference spectrum or not.

An overview of the properties of this method and the results from experiments are also reported in table IX. SFF$^{\mathrm{TM}}$ is also an algorithm included in the ENVI® environment [15].

III. Proposed Method: *Wavanglet*, a spectral angle classification in a wavelet filtered space

The proposed *wavanglet* method is a succession of four steps. Step A is the determination of significant reference spectra E characteristic of the different types of terrains present in the scene (the set is called the "reference base"). Step B is the choice of the most discriminating wavelet subspace for spectral angle (SA) classification of the observed spectra X. Step C is the determination of the best threshold for the spectral angle to produce detection masks (0=non-detection; 1=detection). Step D is the automatic mass classification for the complete dataset.

A. Step A: Choice of relevant reference spectra

This first step is crucial in the process because it will strongly affect the validity of the detection. If some species are not represented in the reference base, they will be misclassified in the dataset. If other species are represented in the base but are not present in the observation, the classification will not be optimized. This method is supervised because the *a priori* knowledge used to perform the classification is strong: number of present compounds in the image, nature of the compounds, etc. The user must supply a reference base that can be a set of end-members extracted from the hyperspectral images and/or a set of synthetic spectra generated by a physical model. End-members can be extracted manually or automatically, for instance by a Pixel Purity Index routine [16], after a dimension reduction performed by different techniques such as Principal Component Analysis (PCA) or Minimum Noise Fraction (MNF) [17]. The synthetic spectra can be calculated with a bidirectional reflectance model adapted to the type of planetary surfaces observed [18]. A single chemical species with homogeneous physical properties (grain size, roughness, etc.) or a geographical/granular mixture of different chemical species with different surface properties may be used under certain circumstances. We will denote the i^{th} spectra of the reference base as E_i. Our algorithm will detect a reference spectrum E_i in an observed spectrum X when the signatures of the former are found in the latter with similar position, width and relative depth. However this method will neither be sensitive to the general level of the spectra nor to the absolute depth of bands for a particular species.

B. Step B: Determination of the best subspace

Several methods have been proposed to reduce the dimension, such as band selection on a well documented learning dataset using discriminant analysis [19], or directly on the hyperspectral image avoiding correlation [20]. We will use the discrete wavelet transform, which is already used to increase the classification accuracy [21], in a alternative way.

B1. Continuum removal: Real observed spectra commonly result from the superposition of multiple absorption bands due to several pure compounds mixed at different spatial scales. Such absorption bands undergo non-linear variations when the physical properties of the materials present in the scene change [22]. Moreover these bands appear on a continuum that is highly variable due to changes of illumination and global albedo. These are the main limiting effects when comparing the observed spectra with the image or synthetic end-members. In order to reduce the sensitivity of our algorithm to such variations - which cannot be taken into account by our fixed reference end-members - we perform the comparison only at medium and small wavelet scales (s$\in$ $[5-8]$ for OMEGA classification). In this first filtered space, all wavelet coefficients mainly depend on the absorption band positions, widths and relative depths. They are only moderately affected

by noise in the spectra as shown by the experiments we carried out (see section IV-C). One specific absorption band is usually represented by several wavelets.

B2. Best discrimination: Additionally we have to select the ideal subspace that allows the best discrimination among the different end-members. It is possible to separate overlapping signatures during the decomposition process if they have different positions or widths, i.e. if we can find one wavelet at medium or small scale, specific to one absorption band but not polluted by another absorption band.

Qualitatively speaking, this subspace is composed of wavelets on which the reference spectra show the greatest differences. We propose three simple methods to carry out the selection:

WE_i(s,p) denotes the projection of the i^{th} spectrum of the reference base on the wavelet $\Psi_{s,p}$ at scale s and position p.

1) Threshold for only one single reference spectra in the base:
   Keep $\Psi_{s,p}$ if $\exists i$ such that
$$\|WE_i(s,p)\| > thres(s) \tag{11}$$
2) Threshold for an extended spectral base:
   Keep $\Psi_{s,p}$ if $\exists(i,j)$ such that
$$\|WE_i(s,p) - WE_j(s,p)\| > thres(s,i,j) \tag{12}$$
   with:
$$thres(s,i,j) = const \tag{13}$$
3) Automatic threshold method, same as method 2 above with:
$$\begin{gathered} thres(s,i,j) = \\ mean_{i,j}\{\|WE_i(s,p) - WE_j(s,p)\|\} \\ +c * std_{i,j}\{\|WE_i(s,p) - WE_j(s,p)\|\} \end{gathered} \tag{14}$$
   Both mean $mean_{i,j}$ and standard deviation $std_{i,j}$ are calculated for combinations of i and j for a given s.
   The coefficient *c* is determined by the user.

The norm $\|\ \|$ can be L^1, L^2, or any other norm definition. We choose L^2 to be consistent with previous considerations concerning wavelet transforms in a **H** Hilbert space (see section II-B).

Methods 1 and 2 cannot easily be carried out if the number of reference spectra is high because the number of thresholds becomes excessive. An alternative is method 3 which automatically determines the threshold. Other more complicated automatic methods have already been proposed in the literature, for example selection of the maximum by scale instead of a threshold criterion [3] or the best basis algorithm [23], [24].

B3. Circularity, noise and dead channels: The first problem that arises when analyzing numerical data by a wavelet transform is the edge effect. The circularity of the sampling creates false information symmetrically before and after the measured signal. All wavelets near the edge are polluted by this construction. To solve such a problem we eliminate all wavelets containing information inherited from the first or last instrument spectels. For the OMEGA images, this method is valid because no features of interest are located near the edge of the signal.

Also wavelets corresponding to spectels affected by instrumental defects or noise can reduce the accuracy of the classification algorithm. These wavelets are determined by the following method. First we built a null-vector with a length equal to the number of spectels in an OMEGA spectrum. Second, we change the value of the vector from zero to one only at the rank of a defective spectel in order to simulate the defect with a normalized energy of one. The base of the modeled defect is denoted D_i. Then we perform a wavelet transform on this signal D_i and eliminate all wavelets with a coefficient higher than a threshold, i.e. the wavelets most affected by the defect. If we choose a typical value of D_i(s,p)>0.5, we eliminate only the wavelets that receive more than 50% of the defect energy. This operation should be performed for all potential defects i.

C. Step C: Spectral angle thresholds

The calculation of the spectral angle (SA) between the reference spectrum E and the observation spectrum X gives the correlation coefficient between these two spectra in a determined space. The characteristics of an appropriate subspace are the following: the belonging wavelets must be corrected from continuum effect (Step B1), form a part of an absorption band and be discriminating for at least one reference spectrum (Step B2) and be almost free of noise and numerical problems (Step B3). The SA in this subspace can be interpreted as a measurement of the agreement between distinctive spectral features of a reference spectrum and those of an observed spectrum. A small value indicates a good match of spectral features whereas a value close to π indicates total disagreement. Some analysis procedures we use subsequently in wavanglet require that we decide from the spectral angle if a given compound, characterized by its associated reference spectrum, is present or absent in a pixel. In this case, after processing the whole image, we obtain detection masks for the compounds that indicate if a given treatment is to be applied or not for a given pixel.

To declare positive detection, the correlation coefficient must be higher than a certain threshold or, in an analogous manner, the spectral angle must be lower than a limiting angle. Ideally, to build our detection algorithm, a unique limiting angle, one per compound, must be detected and valid for all observations. This limiting angle can be interpreted as a limiting condition adapting the mathematical problem to a physical one. Two methods can be performed to determine the series of thresholds: calibration using a controlled database of synthetic spectra - modeling approach [C1] - and/or an empirical approach based on an already analyzed subset of real data [C2]. The choice of the threshold must maximize the detection limit of each pure compound in the image, regardless of its physical properties, and and must minimize false detections.

As the SA calculation is invariant with any linear orthonormal transformation, such as the Daubechies wavelet transform, we have the choice to perform the SA mapping of all the pixels

in the filtered wavelet base or in the filtered spectral space. The latter is reconstructed by the inverse transform of the filtered wavelet base. The calculation of the SA is faster in the filtered wavelet base than in the complete spectral space because the dimensions of the former are lower. We therefore choose to perform the calculation in the filtered wavelet base.

D. Step D: Automatic mass classification with spectral angles in this subspace

All the parameters are now adjusted to perform the automated classification. For each image and each spectrum of the reference base, a detection mask will be created. For datasets spanning a long time range (several months to years), many parameters can vary. For instance the bad channel list can change with time thus affecting steps B2 and B3. If this happens, then step C should be adapted according to the former steps.

IV. Experiments

We will now apply this general *wavanglet* method to a series of OMEGA/MEX hyperspectral images and compare the obtained classifications with the ones produced by two alternative methods: Band Ratio (BR) and Spectral Feature Fitting (SFF) (sections II-C1, II-C3). We also evaluate quantitative detection limits for H_2O and CO_2 ices in terms of abundance. We use synthetic spectra for this. Our study consists of five tests: classification accuracy, separability between classes, multiple end-members and possible overlapping signatures, mass processing feasibility and calculation time.

A. Application of the wavanglet method to the OMEGA dataset

We follow the four steps described in section 3 to apply the method to a collection of OMEGA/MEX images covering the polar regions of Mars.

1) Step A: Choice of relevant "end-members" (reference spectra): The OMEGA spectra display signatures characteristic of both the atmosphere and the surface. The atmospheric contribution is due to gaseous CO_2 and, depending on weather conditions, to clouds of dust, CO_2 and H_2O ices. The spectral effect of the clouds can often be neglected for a first order approximation. The surface contribution is due to a mixture of H_2O ice, CO_2 ice and dust in various proportions. In the images, we try to detect the last 3 compounds to which we attribute reference spectra (see figure 2). Pure H_2O and CO_2 are represented by synthetic spectra computed by a reflectance model [18] using the physical parameters listed in table III and an optical constant measured in the laboratory [25], [26], [27]. These parameters have been chosen to be compatible with recent studies of both south and north martian polar regions [28], [29], [11], [10]. On the other hand, the third reference spectrum representing polar dust is extracted from a single OMEGA image covering the southern high latitudes by averaging all spectra within a relatively homogeneous region near 70° longitude and -77° latitude. Note that this spectrum is almost featureless in the near IR range except for the 3 micron band due to the hydration of the minerals and the absorption bands of atmospheric CO_2. Globally the dust spectrum does not display much spatial variation in this spectral range. Indeed it is well mixed by winds and spread over wide areas. Thus we can assume that our reference spectrum is representative of most areas of both polar regions. Our martian studies focus mainly on the two first end-members while the third end-member represents spectral features that appear in the data but which are not of interest to us.

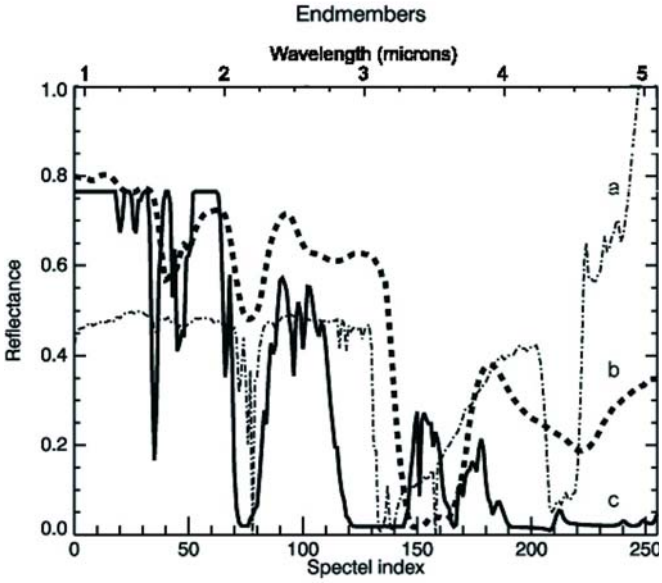

Figure 2. Spectral end-members: dust + atmosphere spectrum (a), synthetic spectrum of H_2O ice (b) and synthetic spectrum of CO_2 ice (c).

Table III
SYNTHETIC END-MEMBER PARAMETERS

	pure H_2O ice	pure CO_2 ice
Grain size (μm)	10	100 000
Incidence angle (°)	85	85
Emergence Angle (°)	0	0

2) Step B: Determination of the best subspace:

B1. Continuum removal: We use only the last four scales (from 5 to 8) in order to remove the contribution of the continuum.

B2. Best discrimination: We prefer the automatic threshold method (method 3), with norm L^2 and the value c=2.5 to select the best subspace. This threshold criterion optimizes the

Table IV
LIST OF ELIMINATED WAVELETS

Spectel indexes of dead spectels	34	78	158
Wavelet indexes of eliminated wavelets	35, 71, 144	82, 166	102, 206

Table V
LIST OF SELECTED WAVELETS

Scale	Indexes of selected wavelets
5	28
6	36, 58
7	73, 80, 95, 118
8	145, 148, 149, 160, 161, 163, 164, 165, 175, 192, 202, 239

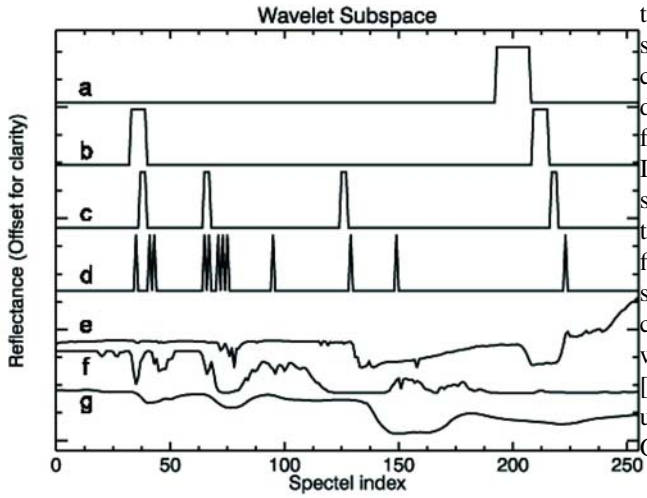

Figure 3. Representation of the selected subspace of wavelets (upper part) that best discriminate the end-members (lower part). Wavelets selected in scales 5 to 8 (a to d). Observed dust and atmosphere spectra (e), synthetic CO_2 ice (f) and synthetic H_2O ice (g). [see section II-B for wavelet representation]

classification.

B3. Circularity, noise and dead spectels: We eliminate all wavelets containing a non-zero contribution from the last spectel # 255.

We eliminate wavelets polluted by damaged spectels (number 34, 78 and 158) with an energy criterion (D=0.45). Table IV lists the indexes of the eliminated wavelets.

Finally the selected subspace is formed by the 12 wavelets shown in figure 3 and summarized in table V.

3) Step C: Threshold determination: We use two different procedures to constrain the spectral angle threshold: numerical calibration [C1] and image calibration [C2]

C1. Numerical calibration: The idea is to generate a database of synthetic spectra that simulates the OMEGA dataset by varying the relative abundances of ices and dust as well as other physical parameters over realistic ranges of values. Then we can apply the *wavanglet* method on this controlled data and adjust the angle threshold so as to maximize the detection sensitivity for H_2O and CO_2 ices while minimizing false detections.

The synthetic spectra are calculated by *SPECTRIMAG*, a bidirectional reflectance model that solves the radiative transfer of solar light through granular icy media [18]. The input data are the spectral optical constants of ice crystals and dust measured in the laboratory [25], [26], [27]. Each compound is also characterized by parameters such as grain size and porosity. A real OMEGA spectrum measures the surface reflectance of a geographical and/or granular mixture of H_2O ice, CO_2 ice and dust at, or under, the pixel scale. In the first case, the resulting spectrum is a linear combination of the spectral reflectance signatures of the individual compounds. In the second case, the spectrum results from non-linear physics aspects implemented in the model. In order to simulate as realistically as possible a martian spectrum acquired by OMEGA, we also take into account the atmosphere and the instrumental noise contributions. The first contribution is introduced by multiplying each simulated spectrum by a constant atmospheric transmission spectrum calculated for an altitude of -4800 m and typical martian weather conditions by a line-by-line radiative transfer model [30]. We simulate the instrumental noise by a Gaussian process using statistics coming from dark current measurements of OMEGA observation 41_1 acquired during orbit 41.

C2. Image calibration: We carry out the training phase of the wavanglet and SFF$^{\mathrm{TM}}$ methods using observation 41_1 that covers the South polar region during local summer (Ls = 337.9 °).

A careful visual interpretation of observation 41_1 was carried out in order to select samples of pixels that we can define as "ground truth" regions of interest (GTROI). Dust, H_2O, and CO_2 ices are identified on the basis of their distinct absorption bands. Nevertheless this operation is very time-consuming and we need as many GTROIs as possible to carry out the training and subsequent testing (see section IV-B) of the classification methods evaluated in this paper. Furthermore the sensitivity of the brain/eye system is sometimes insufficient to recognize relevant spectral features in circumstances such as a very small amount of water ice mixed with solid CO_2. As a consequence we use the limited (≈ 30), manually obtained set of GTROIs for 41_1 in order to train the Band Ratio (BR) method which is always more sensitive than the human eye. We obtain two detection thresholds that respectively separate the CO_2 class from the H_2O class and the latter from the dust class. These thresholds are optimized for observation 41_1 or any other visually interpreted image. Then we consider that the classification maps obtained with this optimized BR

method (hereafter named BR_opt) constitute a reference for the training (observation 41_1) and testing (observation 231_1, see IV-B) of wavanglet as well as other classification methods.

Since our detection classes can overlap because both CO_2 and H_2O ices as well as dust can be detected in the same pixel, the training and testing are performed separately for the three compounds. In each case we consider two classes: pixels with positive detection and pixels with negative detection. For a range of proposed spectral angle thresholds (see Table VII), we calculate the overall accuracy and the kappa statistics [31] given by wavanglet by comparing its classification map with the reference map (BR_opt). The production and user accuracies are also calculated. We retain the threshold that maximizes the kappa factor. The training of SFF is performed in the same manner.

Both numerical and image calibrations converge on threshold angles of 1.54 radian for H_2O ice, 1.48 radian for CO_2 ice, and 0.34 for dust. Note that the threshold value is close to $\pi/2$ for the ices whereas it is much lower for dust. Our reference spectra for H_2O and CO_2 do not contain any atmospheric contribution as opposed to the dust reference and to the images we classify. As a consequence, the observed spectra over icy terrains differ more from their reference spectra than those observed over the dusty terrains. In subsection IV-C, we present the detection limits we achieve on the synthetic spectra in more detail.

4) Step D: Classification using the complete dataset: The presentation and discussion of the results obtained by applying the *wavanglet* method to the complete OMEGA dataset is not the subject of this paper. We only discuss the ability of our algorithm to analyze a selection of representative observations. For that purpose we carry out a comparative study with the BR, SAM$^{\mathrm{TM}}$ and SFF$^{\mathrm{TM}}$ methods (see section II-C).

B. Comparison with other methods

In this paper we illustrate our tests with observation 231_1 of the North polar region recorded during local springtime (Mars solar longitude, Ls = 8.6 °). This observation presents different H_2O and CO_2 ice properties than observation 41_1, such as grain size and dust content [28], [11], [10].

All the results are summarized in table IX.

1) Classification accuracy: We admit that the optimized BR method (BR_opt for 231_1) is the best classification method and thus constitutes a reference (see section IV-A3 C2). Yet we cannot use it to classify the whole OMEGA dataset since it requires the manual constitution of GTROIs and subsequent manual training. As a consequence we only test and compare classification methods that could be used to process a large number of images automatically:

- the non-optimized BR method (hereafter called BR_fix),
- the SFF method,
- and the "Wavanglet" method.

All three methods use fixed detection thresholds to classify the dataset. For BR_fix, the thresholds equal those of BR_opt for observation 41_1.

Table VI shows the overall accuracy of the classifications achieved by *wavanglet*, SFF$^{\mathrm{TM}}$, and BR_fix using the optimized thresholds listed in section IV-A3 . In table VI, note that for the detection of water ice terrains, SFF$^{\mathrm{TM}}$ and wavanglet show similar detection capabilities with an overall accuracy of 86 and 84 % respectively. On the other hand BR_fix misclassifies 64 % of the pixels spectrally dominated by H_2O. For CO_2 terrains, wavanglet clearly outperforms SFF$^{\mathrm{TM}}$ and BR_fix with an overall accuracy of 93 % versus 80%.

2) Separability between classes: Class separability must be considered to evaluate the robustness of a classification algorithm. In our case, each class corresponds to the positive detection of H_2O ice, CO_2 ice and dust. First, we must consider a space in which the data can be represented. For *wavanglet*, this space is the spectral angle in the wavelet filtered subspace, one for each end-member E_i. For the Band Ratio method, this space is the ratio, unique for all end-members. In these representation-spaces, a hyperspectral image is a collection of values, each representing one spectrum. The classification consists in defining a threshold in the distribution of spectral angles or a ratio for the whole population of spectra of a hyperspectral image. The distribution may have three types of groups: first with a dominant presence of the reference material corresponding to E_i (group #1), second with the presence of the same material mixed with other components (group #2), third without the presence of the selected material corresponding to E_i (group #3). In the distribution, each group can be identified and usually multiple peaks correspond to a single group. In our case, the intersection between materials are non-null: for instance we can find materials with both H_2O ice and CO_2 ice (group #2).

The less the intersection between group #2 and group #3 contains pixels, the more the classification will be reliable. One way to estimate the class separability is to evaluate the range of thresholds that give reasonably accurate detections. Robustness is ensured when the range of possible values is relatively wide compared to the width of the groups. This corresponds to a large distance between pixels from groups #2 and #3 in the representative space.

For the Band Ratio method (Fig 4), the H_2O, CO_2 and dust groups strongly overlap and thus the range of possible thresholds is very limited. On the other hand, for the *wavanglet* method (Fig 5), the spectral angle distribution plots of the different materials, measured in their relative representing space, display well separated groups.

3) Multiple end-members and possible overlapping signatures: When an increasing number of end-members is required to classify a large dataset, it must still be possible to separate classes. The band ratio method, as presented above, does not work for the detection of more than a few species because it becomes impossible to find a ratio that ensures class separability, especially when the spectral signatures overlaps. On the other hand, the SFF$^{\mathrm{TM}}$ and *wavanglet* methods are more suitable for the classification of large spectral datasets with multiple end-members because they perform the classification based on an automatically defined spectral subspace. The user only needs to define the end-member collection.

4) Mass processing feasibility: Application of a classification method with a threshold (like *wavanglet*, BR, SFF$^{\mathrm{TM}}$) to a huge dataset requires a constant threshold from one image to the other. Table VII shows the acceptable range of

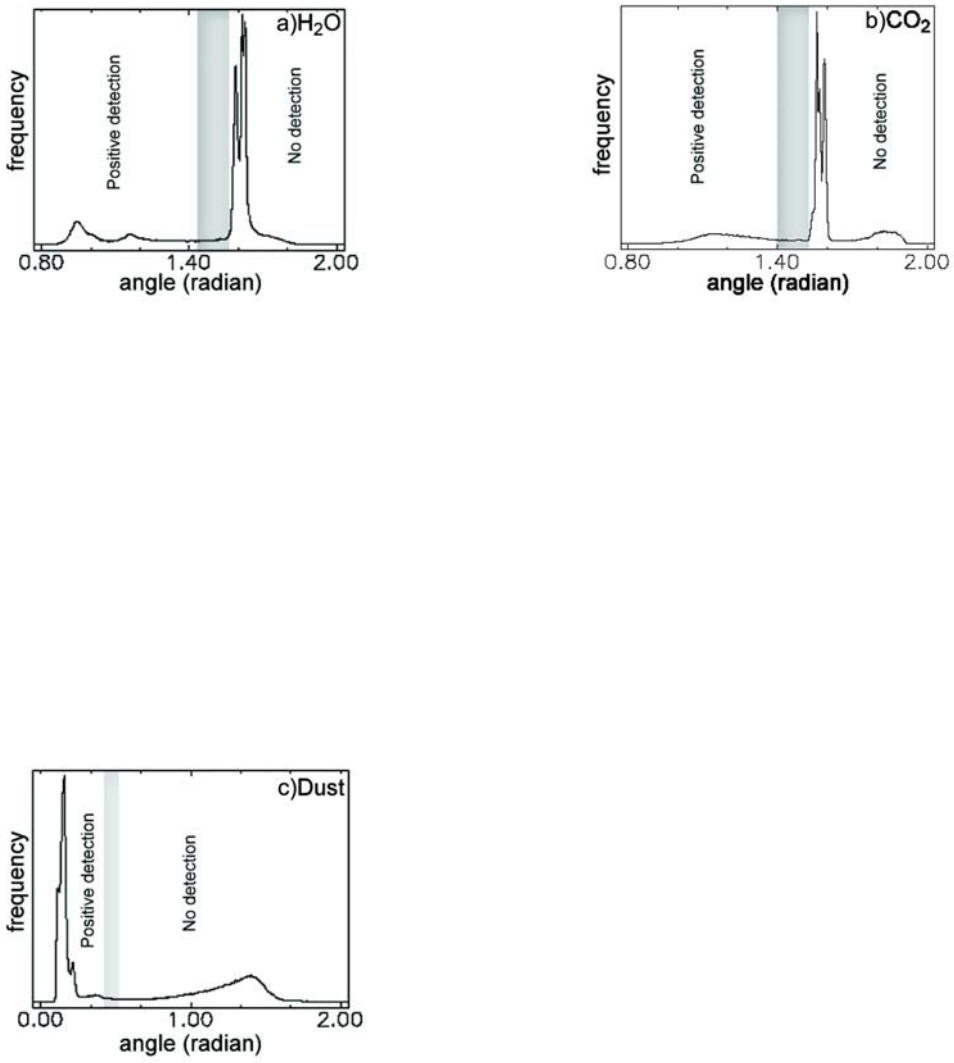

Figure 5. Spectral angle distributions from the *wavanglet* method applied to the 231_1 image for H_2O ice (a), CO_2 ice (b) and dust (c) end-members. The gray box represents the range of acceptable thresholds for reliable detection.

Table VI
CLASSIFICATION ACCURACY FOR A POLAR OBSERVATION (231_1) ACQUIRED BY OMEGA. THE REFERENCE METHOD IS THE BAND RATIO METHOD OPTIMIZED FOR 231_1. THE DEFINITION OF THE KAPPA PARAMETER AND THE OVERALL AND USER ACCURACY CAN BE FOUND IN [31].

Method	Threshold	Kappa	Overall accuracy (%)	user accuracy (%) detection	user accuracy (%) no detection
BR_fix - H_2O	0.36 - 0.664	0.071	35.6	16.8	97.0
SFF^{TM}- H_2O	5.534	0.583	86.0	49.3	99.9
Wavanglet - H_2O	1.54	0.538	83.7	45.3	100.0
BR_fix - CO_2	0.467	0.576	80.2	54.6	100.0
SFF^{TM}- CO_2	3.716	0.572	80.0	54.4	99.9
Wavanglet - CO_2	1.48	0.793	93.2	100	92.0

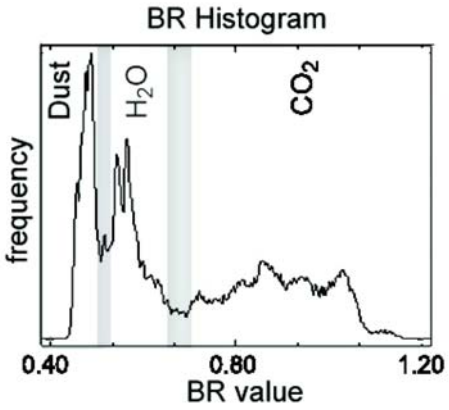

Figure 4. Band Ratio (BR) value distribution for the 231_1 image. The gray boxes represent the range of thresholds possible for Dust/H_2O detection on the right and H_2O/CO_2 detection on the left.

thresholds for the band ratio and *wavanglet methods* based on observations 41_1 and 231_1. For BR, the threshold range between dust and H_2O is strongly variable and automation is therefore not possible. For the *wavanglet* method, the threshold range for a given compound varies only slightly and a single constant value can be selected for optimized detection. The final thresholds determined in section IV-A3 for H_2O, CO_2, and dust are also reported in table VII.

5) Calculation time: We measured the computation time necessary to complete the classification of observation 41_1 (111616 spectra of 256 spectels) with the BR, SFF^{TM} and *wavanglet* methods. A complete process consists of opening files, running the classification algorithm, creating regions of interest and saving product files. Each type of processing was performed in the ENVI® environment on a LINUX workstation with the following characteristics: Intel Xeon 2.40 GHz bi-processor with a 512 KB cache memory for each processor, hyper-threading active technology, 6 GB of RAM, OS Linux with kernel 2.6 SMP. Results of the tests are given in table IX. *Wavanglet* is the slowest method but its run-time is comparable to SFF^{TM}.

C. Evaluating detection limits with synthetic data

We now evaluate the sensitivity of *wavanglet* for the detection of H_2O and CO_2 ices using synthetic data. For this, we consider that solid H_2O, CO_2, and dust form a granular mixture with different mass proportions and grain sizes. For given observation conditions, we calculate the reflectance spectra that OMEGA would measure including the atmosphere contribution and the instrument noise (as explained in IV-A3 C1). We use different sets of parameters in the simulation. We span the whole range of mass proportions in a relatively continuous manner and use a limited set of values for the other parameters: atmospheric path, grain sizes, and incidence angle. The latter values, listed in table VIII, are characteristics of polar ices [28], [29], [11], [10]. For each combination of parameters, we perform automatic detection of the ices using *wavanglet*. The reference base is composed of the three spectra described in section IV-A1 (see fig 2). The results are represented in ternary diagrams with the three poles (H_2O, CO_2, and dust) at the edges of the triangle, one point inside the triangle corresponding to a triplet of mass proportions (their sum being always equal to unity). Each symbol represents a positive detection for a triplet. The absence of symbol means no detection. At one triplet location two symbols can be superimposed on the triangular diagram: the inner and outer symbols correspond to incidence angles of 85° and 15° respectively. We can thus assess the effect of changing the atmospheric path, grain size, and incidence angle on the detection limits.

a) General result: The detection limit for physical parameters of the typical surface (see table VIII) of the permanent South polar cap is plotted in figure 6 and zoomed in figure 7. First, note that the general detection of H_2O ice is good until near the dust corner and near the CO_2 corner. Secondly, the detection of CO_2 ice is only present near the pure CO_2 ice pole. The difference between these two situations is related to

Table VII
THRESHOLD RANGE OF POSITIVE DETECTION FOR THE BAND RATIO AND *wavanglet* METHODS BASED ON 41_1 AND 231_1 OBSERVATIONS.

Threshold	H_2O ice	CO_2 ice	dust
BR_opt on 41_1	<0.360 (*<0.398*) to >0.467 (>0.664)	>0.467 to >0.664	<0.360 to *<0.398*
BR_opt on 231_1	*<0.507* (<0.532) to >0.651 (>0.695)	>0.651 to >0.695	*<0.507* to <0.532
wavanglet opt. on 41_1	<1.5 to <1.56	<1.4 to <1.53	<0.3 to <0.6
wavanglet opt. on 231_1	<1.45 to <1.57	<1.43 to <1.52	<0.32 to <0.58
operational wavanglet	<1.54	<1.48	<0.34

the grain size effect. The grain size of CO_2 ice is almost 500 times greater than the grain size of H_2O ice and 1000 times greater than that of dust. In our case of granular mix, the mean free path is smaller inside CO_2 ice than inside H_2O ice or dust. The result is that even with a similar proportion of H_2O, CO_2 and dust, the CO_2 absorption bands will be smaller than the H_2O and dust absorption bands. The presence of significant CO_2 absorption bands in the spectra requires a high relative weight proportion of CO_2 in order to balance this grain size effect.

b) Atmospheric path: We generate two ternary diagrams for an atmosphere extending from space to an altitude of respectively + 4800 m (a situation typical of South polar region of Mars, fig 6) and - 4800 m (a situation typical of the northern lowland region, fig 8). We see in the figures that, despite a large atmosphere thickness difference, the atmospheric path has only a minor effect on our detection limits. The detection of ice with the *wavanglet* method is thus only slightly disturbed by the atmosphere contribution.

c) Grain size effect: Two ternary diagrams are calculated, one with a water ice grain size of 100 μm (fig 6), a value characteristics of the permanent South polar cap [28], [29], [10] and a second with a much higher value (1000 μm, North polar Cap [11], fig 9). Comparison of the two figures shows that the detection capacity strongly decreases as the grain size departs from the one used to generate the reference spectrum ($10\mu m$). This effect is due to the high non-linear dependence of the H_2O and CO_2 spectral signatures with grain size that *wavanglet* cannot handle. In conclusion, for efficient detection, the real grain size on the site must not be too different from the value used for the end-member reference. Otherwise we must modify or complete our reference base with more relevant spectra (simulated, measured or observed) in order to improve the detection limit.

d) Incidence angle: For a first approximation, the observation parameters (incidence, emergence and azimuth angles) only influence the absolute band depth of the spectral features. Since the *wavanglet* classification method is mostly sensitive to relative band depth, it may be fairly independent with respect to the illumination and observation conditions. The effect of the incidence angle has been tested for two extreme values: 85° (inner symbols) and 15° (outer symbols) for all the previous parameter sets (figures 6, 8, 9 and 7). The relative positioning of the inner and outer symbols for H_2O and CO_2 in all figures shows a very slightly better detection limit for 15° incidence. Other calculations on the emergence angle near the nadir support the same conclusion. The *wavanglet* method appears to be independent of the geometrical conditions of the observation.

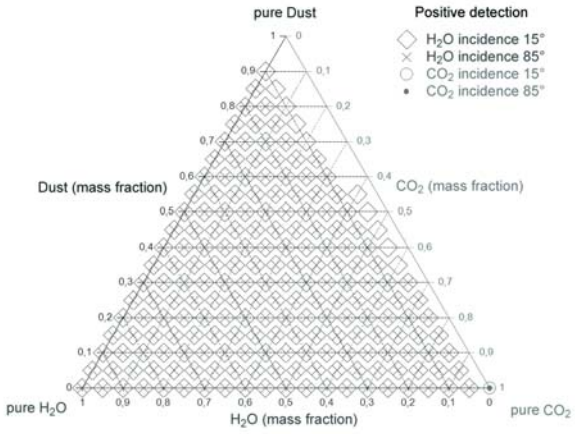

Figure 6. Detection limits for H_2O and CO_2 for physical parameters of the typical surface (see table VIII) of the permanent South polar cap. The atmosphere is typical for these conditions. The type of mixing is granular. Each symbol corresponds to positive detection of H_2O ice (square and cross) and CO_2 ice (circle and dot).

V. DISCUSSION AND CONCLUSION

We have conducted a comparative study between two generic methods - the Band Ratio method (BR) and Spectral Feature Fitting (SFF$^{\mathrm{TM}}$) - and *wavanglet*, our wavelet based procedure. For this, we have considered five criteria pertaining to automatic compound detection and classification of spectra: overall accuracy, separability between classes, multiple end-members and possible overlapping signatures, mass processing feasibility and calculation time. Table IX shows that only *wavanglet* possesses all the desired properties. Furthermore it has the highest overall accuracy, outperforming SFF$^{\mathrm{TM}}$ for the

Table VIII
SET OF PHYSICAL AND OBSERVATION PARAMETER VALUES USED TO GENERATE THE TERNARY COMPOSITION DIAGRAMS

	Figure 6 and 7	Figure 8	Figure 9
Grain size H_2O ice (μm)	100	100	**1000**
Grain size CO_2 ice (μm)	45 000	45 000	45 000
Grain size dust (μm)	30	30	30
Incidence angle (°)	85 and 15	85 and 15	85 and 15
Emergence angle (°)	0	0	0
Atmosphere	South	**North (deeper)**	South

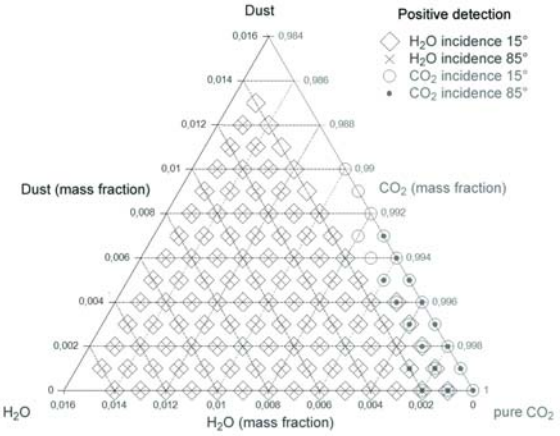

Figure 7. Zoom on the lower right corner (pure CO_2) of figure 6. Each symbol corresponds to positive detection of H_2O ice (square and cross) and CO_2 ice (circle and dot).

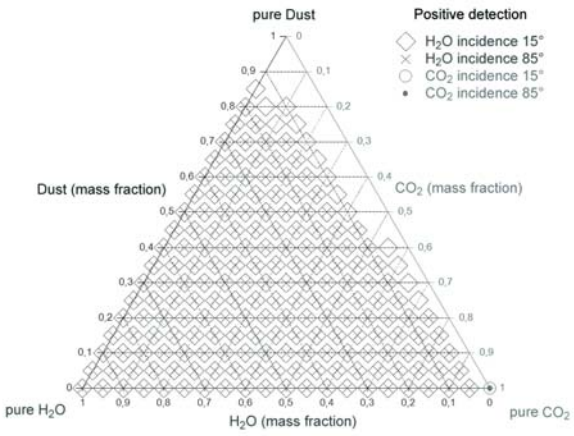

Figure 8. Same conditions as in figure 6 except for a larger atmospheric path. Each symbol correspond to a positive detection of H_2O ice (square and cross) and CO_2 ice (circle and dot). Table VIII summarizes all parameters.

CO_2 terrains. The BR_fix method usually mis-classified a large fraction of the OMEGA images and unfortunately BR_opt is not suitable for mass processing of complete datasets because a unique single detection threshold cannot be determined and applied to all OMEGA images. Also, BR is potentially very sensitive to noise for some spectels. Furthermore *wavanglet* has two interesting properties for classifying our dataset: a reasonable calculation time and possible multidetections with a large end-member dataset. We demonstrated that the *wavanglet* method is able to discriminate between various spectral patterns that sometimes differ insufficiently and strongly overlap. We have also evaluated the sensitivity of *wavanglet* for the detection of H_2O and CO_2 ices as a function of certain physical as well as geometrical parameters using synthetic data. Thanks to the selection of medium and small scale wavelets, the sensitivity of *wavanglet* is not hampered by variations of the incidence and emergence angles or by noise. Furthermore, the presence of atmospheric CO_2 bands has a minor influence on detection. On the other hand, the non-linear effect of grain size variability on the spectral signatures is difficult to handle with only one reference spectrum per material. To improve detectability over a wide range of surface textures, we propose selection of one end-member per terrain and per characteristic grain size in the reference base.

Table IX
COMPARISON OF BAND RATIO, SPECTRAL FEATURE FITTING AND *wavanglet* METHODS

	Band Ratio (BR_fix)	Spectral Feature Fitting	*Wavanglet*
Overall accuracy (mean for H_2O and CO_2)	57%	83%	**89%**
Class separability	Low	Overlap	**High**
Large end-member dataset	Difficult	**Possible**	**Possible**
Mass processing	Yes (No for BR_opt)	-	**Yes**
Calculation time (s)	**11**	41	54
Noise dependence	High and localized	-	**Low**

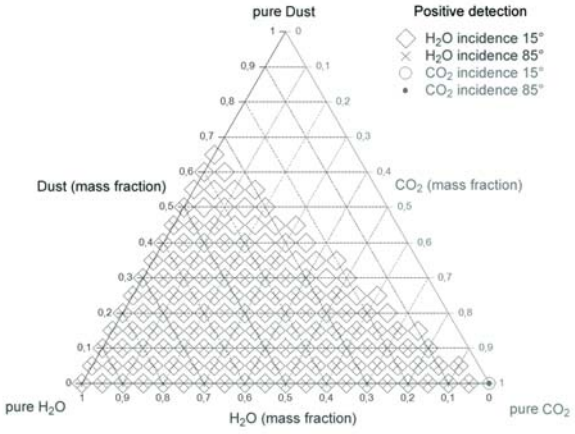

Figure 9. Same conditions as in figure 6 except for a larger water grain size (1000 μm) compared to the reference on the detection limits (100 μm). Each symbol corresponds to positive detection of H_2O ice (square and cross) and CO_2 ice (circle and dot). Table VIII summarizes all parameters.

VI. ACKNOWLEDGMENT

We thank two anonymous reviewers for interesting remarks. This work is supported by a PhD grant from the 'Ministère délégué à l'Enseignement supérieur et à la Recherche' and by a contract with CNES through its 'Groupe Système Solaire' programs. We thank the OMEGA team at IAS for support with sequencing and data downloading activities. We also thank Mathieu Lonjaret, Fabrice Madec and Thomas Questier for usefull discussions.

REFERENCES

[1] J.-P. Bibring, A. Soufflot, M. Berthé, Y. Langevin, B. Gondet, P. Drossart, M. Bouyé, M. Combes, P. Puget, A. Semery, G. Bellucci, V. Formisano, V. Moroz, V. Kottsov, G. Bonello, S. Erard, O. Forni, A. Gendrin, N. Manaud, F. Poulet, G. Poulleau, T. Encrenaz, T. Fouchet, R. Melchiori, F. Altieri, N. Ignatiev, D. Titov, L. Zasova, A. Coradini, F. Capacionni, P. Cerroni, S. Fonti, N. Mangold, P. Pinet, B. Schmitt, C. Sotin, E. Hauber, H. Hoffmann, R. Jaumann, U. Keller, R. Arvidson, J. Mustard, and F. Forget, *OMEGA: Observatoire pour la Minéralogie, l'Eau, les Glaces et l'Activité*. ESA SP-1240: Mars Express: the Scientific Payload, Aug. 2004, pp. 37–49.

[2] F. A. Kruse, A. B. Lefkoff, J. W. Boardman, K. B. Heidebrecht, A. T. Shapiro, P. J. Barloon, and A. F. H. Goetz, "The spectral image processing system (sips)–interactive visualization and analysis of imaging spectrometer data," *Remote Sensing of Environment*, vol. 44, pp. 145–163, May 1993.

[3] N. S. Subotic, J. D. Gorman, and B. J. Thelen, "Wavelet techniques for band selection and material classification from hyperspectral data," in *Proc. SPIE Vol. 2480, p. 426-434, Imaging Spectrometry, Michael R. Descour; Jonathan M. Mooney; David L. Perry; Luanna R. Illing; Eds.*, Jun. 1995, pp. 426–434.

[4] L. M. Bruce and J. Li, "Fast wavelet-based algorithms for multiresolutional decomposition and feature extraction of hyperspectral signatures," in *Proc. SPIE Vol. 3717, p. 72-81, Algorithms for Multispectral and Hyperspectral Imagery V, Sylvia S. Shen; Michael R. Descour; Eds.*, Jul. 1999, pp. 72–81.

[5] L. M. Bruce, C. H. Koger, and J. Li, "Dimensionality reduction of hyperspectral data using discrete wavelet transform feature extraction," *IEEE Transactions on Geoscience and Remote Sensing*, vol. 40, pp. 2331–2338, 2002.

[6] S. Kaewpijit, J. Le Moigne, and T. El-Ghazawi, "Automatic reduction of hyperspectral imagery using wavelet spectral analysis," *IEEE Transactions on Geoscience and Remote Sensing*, vol. 41, pp. 863–871, 2003.

[7] C. H. Koger, L. M. Bruce, D. R. Shaw, and K. N. Reddy, "Wavelet analysis of hyperspectral reflectance data for detecting pitted morningglory (ipomoea lacunosa) in soybean (glycine max)," *Remote Sensing of Environment*, vol. 86, pp. 108–119, June 2003.

[8] H. Wu, G. Kuang, and W. Yu, "Unsupervised classification method for hyperspectral image combining PCA and Gaussian mixture model," in *Third International Symposium on Multispectral Image Processing and Pattern Recognition. Edited by Lu, Hanqing; Zhang, Tianxu. Proceedings of the SPIE, Volume 5286, pp. 729-734 (2003).*, H. Lu and T. Zhang, Eds., Sep. 2003, pp. 729–734.

[9] J. E. Pinzon, S. L. Ustin, C. M. Castaneda, J. F. Pierce, and L. A. Costick, "Robust spatial and spectral feature extraction for multispectral and hyperspectral imagery," in *Proc. SPIE Vol. 3372, p. 199-210, Algorithms for Multispectral and Hyperspectral Imagery IV, Sylvia S. Shen; Michael R. Descour; Eds.*, S. S. Shen and M. R. Descour, Eds., Jul. 1998, pp. 199–210.

[10] J. Bibring, Y. Langevin, F. Poulet, A. Gendrin, B. Gondet, M. Berthé, A. Soufflot, P. Drossart, M. Combes, G. Bellucci, V. Moroz, N. Mangold, B. Schmitt, and t. OMEGA team, "Perennial water ice identified in the south polar cap of Mars," *Nature*, vol. 428, pp. 627–630, Apr. 2004.

[11] Y. Langevin, F. Poulet, J.-P. Bibring, B. Schmitt, S. Douté, and B. Gondet, "Summer Evolution of the North Polar Cap of Mars as Observed by OMEGA/Mars Express," *Science*, vol. 307, pp. 1581–1584, Mar. 2005.

[12] R. N. Clark, A. J. Gallagher, and G. A. Swayze, "Material absorption band depth mapping of imaging spectrometer data using the complete band shape leastsquares algorithm simultaneously fit to multiple spectral features from multiple materials," in *Proceedings of the Third Airborne*

Visible/Infrared Imaging Spectrometer (AVIRIS) Workshop, JPL Publication 90-54, 1990, pp. 176–186.

[13] S. Mallat, *A Wavelet Tour of Signal Processing*. Academic Press, 1999, ch. 4, pp. 107–121.

[14] W. H. Press, B. P. Flannery, S. A. Teukolsky, and W. T. Vetterling, *Numerical Recipes in Fortran 77 : the art of scientific computing*. Cambridge University Press, 1986-1992, ch. 13.10, pp. 584–599.

[15] *ENVI User's Guide*. Research Systems, 2000, ch. 9 : Spectral Tools, pp. 615–686.

[16] J. Boardman, F. A. Kruse, and R. O. Green, "Mapping target signatures via partial unmixing of AVIRIS data: in Summaries," in *Fifth JPL Airborne Earth Science Workshop, JPL Publication 95-1*, vol. 1, Mar. 1995, pp. 23–26.

[17] A. Green, M. Berman, P. Switzer, and M. Craig, "A transformation for ordering multispectral data in terms of image quality with implications for noise removal," *IEEE Transactions on Geoscience and Remote Sensing*, vol. 26, no. 1, pp. 65–74, 1988.

[18] S. Douté and B. Schmitt, "A multilayer bidirectional reflectance model for the analysis of planetary surface hyperspectral images at visible and near-infrared wavelengths," *Journal of Geophysical Research*, vol. 103, no. 12, pp. 31 367–31 390, Dec. 1998.

[19] L. Renzullo, A. Blanchfield, and K. Powell, "A method of wavelength selection and spectral discrimination of hyperspectral reflectance spectrometry," *Geoscience and Remote Sensing, IEEE Transactions on*, vol. 44, no. 7, pp. 1986–1994, 2006.

[20] C.-I. Chang and S. Wang, "Constrained band selection for hyperspectral imagery," *Geoscience and Remote Sensing, IEEE Transactions on*, vol. 44, no. 6, pp. 1575–1585, 2006.

[21] J. Li, "Wavelet-based feature extraction for improved endmember abundance estimation in linear unmixing of hyperspectral signals," *Geoscience and Remote Sensing, IEEE Transactions on*, vol. 42, no. 3, pp. 644–649, 2004.

[22] S. Liangrocapart and M. Petrou, "Feasibility study on the use of nonlinear spectral unmixing," in *Proc. SPIE Vol. 3871, p. 159-168, Image and Signal Processing for Remote Sensing V, Sebastiano B. Serpico; Ed.*, Dec. 1999, pp. 159–168.

[23] R. R. Coifman and M. V. Wickerhauser, "Entropy-based algorithms for best basis selection," *IEEE Transactions on Information Theory*, vol. 38, pp. 713–718, 1992.

[24] N. Saito and R. R. Coifman, "Local discriminant bases," in *Proc. SPIE Vol. 2303, p. 2-14, Wavelet Applications in Signal and Image Processing II, Andrew F. Laine; Michael A. Unser; Eds.*, Oct. 1994, pp. 2–14.

[25] E. Quirico and B. Schmitt, "Near-Infrared Spectroscopy of Simple Hydrocarbons and Carbon Oxides Diluted in Solid N_2 and as Pure Ices: Implications for Triton and Pluto," *Icarus*, vol. 127, pp. 354–378, Jun. 1997.

[26] W. M. Grundy and B. Schmitt, "The temperature-dependent near-infrared absorption spectrum of hexagonal H_2O ice," *Journal of Geophysical Research*, vol. 103, pp. 25 809–25 822, Nov. 1998.

[27] B. Schmitt, E. Quirico, F. Trotta, and W. M. Grundy, "Optical Properties of Ices from UV to Infrared," in *ASSL Vol. 227: Solar System Ices*, 1998, pp. 199–240.

[28] S. Douté, B. Schmitt, Y. Langevin, J.-P. Bibring, F. Altieri, G. Bellucci, B. Gondet, and the MEX OMEGA Team, "South Pole of Mars: Nature and Composition of the Icy Terrains from Mars Express OMEGA Observations," *Planetary and Space Sience, in press*.

[29] D. A. Glenar, G. Hansen, G. Bjoraker, M. Smith, J. Pearl, and D. Blaney, "Bright-region radiative properties within the Mars south polar cap (Ls=231) from near-infrared spectroscopic imaging," *Icarus*, vol. 174, pp. 600–603, Apr. 2005.

[30] S. A. Clough, M. W. Shephard, E. J. Mlawer, J. S. Delamere, M. J. Iacono, K. Cady-Pereira, S. Boukabara, and P. D. Brown, "Atmospheric radiative transfer modeling: a summary of the AER codes [rapid communication]," *Journal of Quantitative Spectroscopy and Radiative Transfer*, vol. 91, pp. 233–244, Mar. 2005.

[31] R. Congalton and K. Green, *Assessing the accuracy of remotely sensed data: principles and practices*, J. Lyon, Ed. Lewis Publishers, 1999.